Ab initio study of antiphase boundaries and stacking faults in L12 and DO22 compounds

Rosengaard, N. M.; Skriver, Hans Lomholt

Published in:
Physical Review B Condensed Matter

Link to article, DOI:
10.1103/PhysRevB.50.4848

Publication date:
1994

Document Version
Publisher's PDF, also known as Version of record

Citation (APA):
Rosengaard, N. M., & Skriver, H. L. (1994). Ab initio study of antiphase boundaries and stacking faults in L12 and DO22 compounds. Physical Review B Condensed Matter, 50(7), 4848-4858. DOI: 10.1103/PhysRevB.50.4848

PHYSICAL REVIEW B VOLUME 50, NUMBER 7 15 AUGUST 1994-I

Ab initio study of antiphase boundaries and stacking faults in $L1_2$ and DO_{22} compounds

N. M. Rosengaard* and H. L. Skriver
Center for Atomic-scale Materials Physics and Physics Department,
Technical University of Denmark, DK-2800 Lyngby, Denmark

(Received 6 April 1994)

We have performed *ab initio* calculations of the energies of antiphase boundaries as well as complex and superlattice intrinsic stacking faults in nine intermetallic compounds observed in the face-centered-cubic $L1_2$ and DO_{22} structures. The calculations were performed by means of a Green's function technique based on the linear-muffin-tin-orbitals method within the tight-binding and atomic-sphere approximations.

I. INTRODUCTION

A large class of ordered A_3B compounds forms in the $L1_2$ structure, which is a superlattice based on a face-centered-cubic (fcc) structure, where the minority B atoms occupy one of the four possible basis positions. As a result of the cubic symmetry the compounds in the $L1_2$ structure possess the maximum number of slip systems and often exhibit ductile behavior. A different class of A_3B compounds forms in the tetragonal DO_{22} structure, which is also a superlattice based on the fcc structure. Typically, the ordering tendency of such transition-metal compounds has been related to the electron to atom ratio.[1] Empirically one finds that in compounds with more than 8.65 electrons per atom the minority atoms occupy a simple rectangular lattice within each close-packed layer, while in compounds with fewer than 8.65 electrons per atom the minority atoms occupy a honeycomb structure within the close-packed layers. For fcc based compounds the first case leads to the tetragonal DO_{22} structure and the second to the cubic $L1_2$ structure. In contrast to the $L1_2$ compounds, intermetallics in the DO_{22} structure are often observed to be less ductile and this is conventionally ascribed to the lower symmetry resulting in fewer equivalent split systems.

The mechanical properties of ordered A_3B compounds are affected by the existence of superdislocations[2–5] and by the formation of extended superdislocations, which consists of partial dislocations bounding stacking faults or antiphase boundaries (APB's). It turns out that the energies involved in the formation of these antiphase boundaries and stacking faults are instrumental in most theories of the yield behavior of ordered intermetallics. In particular, the ratio of different fault energies is a parameter which affects the relative stability of the core structures of various extended dislocations.[6] However, as pointed out by Yoo,[7] also elastic anisotropy effects play an important role in determining the core structure of extended dislocations. Recent theories of the yield stress behavior and the dislocation core structure of $L1_2$ intermetallics has been summarized by Sun and Hazzledine,[5] who also reference most of the previous work.

In the context of extended dislocations, the stacking faults most commonly encountered are the superlattice intrinsic stacking fault (SISF) and the complex stacking fault (CSF), which both cause an intrinsic stacking fault in the underlying fcc lattice. The two types of faults differ in that the SISF conserves the nearest neighbors of all the atoms whereas the CSF causes minority atoms to become nearest neighbors. The APB's found in connection with the extended dislocations are the plane boundaries between domains in which the minority atoms occupy different basis positions in the unit cell. In contrast to the stacking and twin faults, they preserve the fcc lattice.

It is possible with some caution to estimate the energies of extended faults from experimental observations, but the values obtained may depend on the models used in the interpretation. In this situation it is important to be able to obtain the faults energies from theoretical calculations. In the past there have been a number of such calculations, most notably the full potential calculations by Paxton[3] and Fu *et al.*,[8] who used a supercell geometry to describe the extended faults. In the present study, we apply a linear-muffin-tin-orbitals (LMTO) interface Green's function technique,[9] which has the advantage over the supercell approach in that it gives the energy of a single fault in an infinite medium. It is, on the other hand, based on the atomic-sphere approximation (ASA) and does not include the effect of relaxation of the surface geometry. The method has, however, proven to be highly accurate in calculations of surface energies[10] and stacking fault energies[11] of metals as well as exchange interaction in magnetic multilayers.[12]

Here we present calculations of the antiphase boundary energies related to close-packed (111) and cube (001) planes as well as the energies of the complex and superlattice intrinsic stacking faults. The calculations were performed for six intermetallics observed in the cubic $L1_2$ structure and three intermetallics in the tetragonal DO_{22} structure. In the cause of the calculations we encountered a few compounds where the antiphase boundary energies were negative and these will be presented in a study of the formation of long-period superstructures.[13]

A. Experiment

The experimental determination of APB and stacking fault energies of intermetallic compounds are based on observation of partial dislocations by transmission electron microscopy (TEM). The field has recently been reviewed by Veyssière,[14] who also discusses the accuracy of TEM determination of APB's and the difficulties connected with the interpretation of dislocation images. Furthermore, the experimental determination of fault energies requires knowledge of elastic constants, and the energies derived depend on the type of elasticity theory applied. Douin *et al.*[15] reported a dramatic reduction of the APB energies of Ni_3Al when elastic anisotropy was included in the calculation.

In the case of APB's a further complication is caused by the possibility of an APB spreading onto other crystal planes. This may not be detected by TEM. A number of workers have pointed out the importance of chemical relaxation, i.e., local disorder near APB's. This subject has been reviewed by Morris.[16] The effect of chemical relaxation is to cause a temperature-dependent decrease in the observed APB energy from its low temperature value. Chemical relaxation may be important already at temperatures well below the ordering temperature.

Similar to the determination of stacking fault energies in elemental metals, the determination by TEM of APB's and stacking faults in ordered compounds is especially difficult when the fault energies are high. The experimentally determined APB and stacking fault energies have been collected by Veyssière,[14] who also cites most of the previous work. It may be noted that the majority of observations of APB's and stacking faults in intermetallics have been performed for Ni_3Al.

B. Theory

Recent theoretical work on stacking faults and antiphase boundaries in $L1_2$ intermetallics include the local-density calculations by Paxton,[3] who used the full potential (FP) LMTO method in the supercell approach to calculate fault energies on close-packed planes in the compounds Cu_3Au, Pt_3Al, and Ni_3Al. Fu *et al.*[8] used the full potential linearized augmented plane wave (FLAPW) method to calculate the (001) and (111) APB energies and the CSF and SISF energies in Ni_3Si and Ni_3Al. Pei *et al.*[17] extracted (001) APB energies for Co_3Ti in the $L1_2$ and Ni_3V in the DO_{22} structures from a LMTO ASA calculation of structural energy differences. In a study of the influence of chemical order on dislocation structure, Dimiduk *et al.*[18] calculated the (111) APB and the CSF energies in Ni_3Al by means of the embedded atom method. In a study of dislocations and grain boundaries, Vitek *et al.*[19] calculated (001) APB, (111) APB, and stacking fault energies in Cu_3Au and Ni_3Al by employing an empirical potential of the Finnis-Sinclair type.

II. GEOMETRY

Below we shall briefly outline the geometry of the antiphase boundaries and stacking faults for which we have calculated the energy of formation by the interface Green's function technique. To do so, we follow the work of Amelinckx,[2] Paxton,[3] and Yamaguchi *et al.*[4]

An antiphase boundary may be viewed as the plane boundary between regions with perfect order. However, as a consequence of the degeneracy with respect to A and B occupation of the underlying lattice, the superstructure within each region may not match. Hence APB's may form as a consequence of an ordering process, where identical atoms occupy different sublattices in different regions of space. From a formal point of view, APB's may be constructed by translating the atoms on one side of the APB plane relative to the atoms on the other side, by the fault or shearing vector, which is a lattice vector of the underlying close-packed crystal structure, but not of the superlattice. The APB's described by a translation vector are of the so-called conservative type, as opposed to nonconservative APB's which may only be formed by removing a number of atomic layers. As a result, the nonconservative APB may alter the stoichiometry locally. In the present study, we will consider only conservative APB's, the energies of which are determined solely by changes in the chemical environment of the atoms near the APB.

APB's are observed not only as defects in growth processes but also in the splitting of superdislocations formed in the mechanical deformation of a solid. In the latter context, the APB is formed when a dislocation splits into superpartials in the process

$$[0\bar{1}1] \rightarrow \frac{1}{2}[0\bar{1}1] + \frac{1}{2}[0\bar{1}1], \tag{1}$$

where the superpartials on the right-hand side of the reaction are separated by an antiphase boundary. In the $L1_2$ structure, both the (001) and (111) APB's have the fault vector $\frac{1}{2}a[01\bar{1}]$, where a is the lattice spacing.

In Fig. 1 the atomic positions in a close-packed plane is shown schematically and the positions of the minority

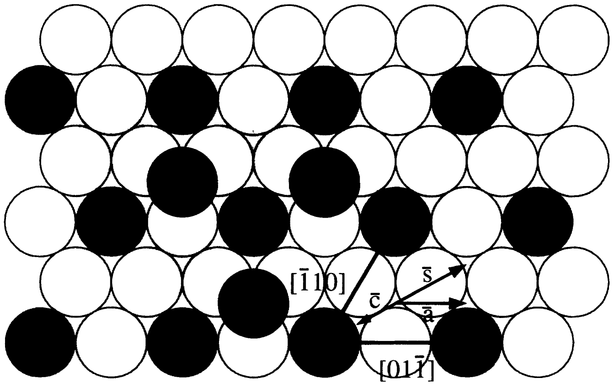

FIG. 1. Close-packed plane in the $L1_2$ structure. Shaded circles indicate the position of minority atoms, while open circles denote the position of majority atoms. Light shaded circles and dark circles indicate position of minority atoms in the close-packed layers below and above. Fault vectors of the (111) APB, the complex (CSF), and superlattice intrinsic (SISF) stacking faults are shown as $\bar{a}$, $\bar{c}$, and $\bar{s}$, respectively.

atoms in the adjacent close-packed layers are sketched. It may be seen from the figure that no minority atoms are nearest neighbors in the $L1_2$ structure. An APB on a close-packed plane is formed by moving all layers above the close-packed layer by the vector **a** in the figure. This shear operation causes minority atoms to become nearest neighbors, as may be seen from the figure, where translation of dark spheres by the vector **a** brings dark and shaded spheres into contact.

The superlattice intrinsic stacking fault is the planar fault formed by translating all atoms above an arbitrary close-packed plane by the fault vector $\frac{1}{3}a[\bar{1}2\bar{1}]$, indicated in Fig. 1 as vector **s**. This shear operation causes an intrinsic fault in the underlying fcc crystal, while the nearest neighbors are conserved for all atoms. Similarly, the complex stacking fault is formed on a close-packed plane by a translation which produces an intrinsic stacking fault in the underlying fcc crystal. In this case the fault vector **c** is $\frac{1}{6}a[1\bar{2}1]$. Because of the superstructure, the CSF causes minority atoms in the close-packed planes nearest to the fault plane to become nearest neighbors.

The CSF is observed in the further splitting of the superpartial described in (1) by the Burgers or APB fault vector $\frac{1}{2}a[0\bar{1}1]$. This splitting is analogous to the splitting of a dislocation in an elemental fcc metal into Shockley partials and may be described by the process

$$\frac{1}{2}a[0\bar{1}1] \rightarrow \frac{1}{6}a[1\bar{2}1] + \frac{1}{6}a[\bar{1}\bar{1}2], \tag{2}$$

where the complex stacking fault is formed between the Shockley partials on the right-hand side of the reaction.

The SISF is formed in a process similar to the one causing the CSF. In fact, multiplying (2) by 2 gives a splitting reaction for a superlattice dislocation. The extended dislocation formed by this reaction consists of a SISF separated by partials which have Burgers vectors $2 \times \frac{1}{6}a[\bar{1}2\bar{1}]$, i.e., twice that for a Shockley partial.

In the $L1_2$ crystal structure illustrated in Fig. 2 all minority atoms have only majority atoms as nearest neighbors. Since the stacking sequence along the [001] axis consists of alternating planes of a square lattice occupied by either A atoms only or by A and B atoms, all atoms maintain their nearest neighbors at the APB with fault vector $\frac{1}{2}a[01\bar{1}]$ on a cube plane. This is in contrast to the APB on a close-packed plane. The effect of applying $\frac{1}{2}a[01\bar{1}]$ to a cube plane is an interchange of the minority and majority atoms in each mixed plane above the APB plane. Since nearest neighbors are conserved in the (001) APB, one may, for strongly ordered intermetallics, expect the (111) APB energy to be larger than the (001) APB energy. This, at least, will be the case whenever ordering can be assigned to a repulsive pair interaction between the minority atoms.

The DO_{22} crystal structure may be formed from the $L1_2$ structure by translating every second mixed plane along the (001) direction by the APB shearing vector. This is equivalent to interchanging the position of the minority and the majority atom within every second cube plane. On the close-packed planes of the DO_{22} structure, the minority atoms form a primitive rectangular unit cell; see Fig. 3. Consequently, we cannot use the same shearing vectors to define the stacking faults. We will describe the intrinsic stacking fault also containing a chemical fault as a CSF in the DO_{22} structure, while the intrinsic stacking fault that preserves nearest neighbors will be denoted the intrinsic stacking fault (ISF). Shearing vectors for the two types of stacking faults are denoted $\bar{s}$ and $\bar{c}$, respectively. As a consequence of the reduced symmetry of the rectangular unit cell, the DO_{22} structure contains two different APB's on the close-packed planes. We will refer to the APB's related to $\bar{a}_1$ and $\bar{a}_2$ in Fig. 3 as APB_1 and APB_2, respectively, thus matching the definitions used by François *et al.*[20] in their study of Ni_3V in

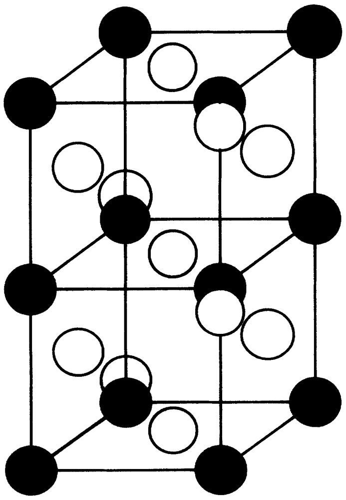

FIG. 2. Two unit cells of the $L1_2$ crystal structure stacked along the [001] cube axis. Filled spheres indicate the position of minority atoms and open spheres indicate the position of majority atoms. Viewed along the cube axis every second layer consists of majority atoms only.

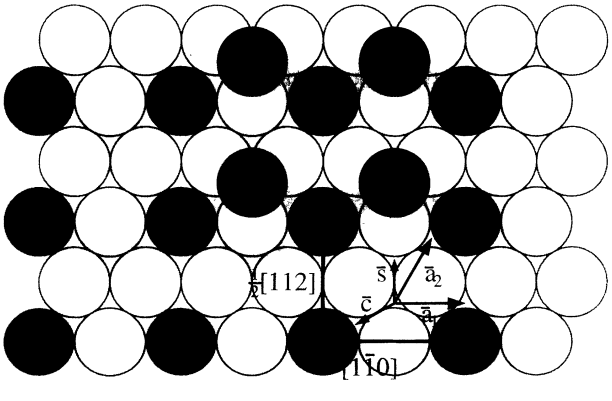

FIG. 3. Close-packed plane in the DO_{22} structure. Shaded circles indicate the position of minority atoms, while open circles denote the position of majority atoms. Light shaded circles and dark circles indicate position of minority atoms in the close-packed layers below and above. Fault vectors of the (111) APB's, the complex (CSF), and the simple intrinsic (ISF) stacking faults are shown as $\bar{a}_1$, $\bar{a}_2$, $\bar{c}$, and $\bar{s}$, respectively. The two lattice vectors shown represent Burgers vectors for observed superdislocations.

the DO_{22} structure. These authors also describe the observed core structures of the two most common extended superdislocations which have the Burgers vectors $\frac{1}{2}a[112]$ and $a[1\bar{1}0]$ shown in Fig. 3.

III. METHOD OF CALCULATION

The calculations were performed by means of the tight-binding LMTO Green's function technique,[9–11] which is based on the work of Andersen and co-workers.[21–27] An essential aspect of the technique is the ability, within the ASA and in the tight-binding representation, to generate the Green's function matrices for a real, two-dimensional interface by a simple and efficient procedure. The original implementation is described in Ref. 9 and the technique was later improved by the introduction of linear response theory and a linearized Dyson equation, which reduced the number of time-consuming iterations considerably.[10,11]

Recently we implemented the so-called principal layer technique[28] to calculate the ideal Green's function. This technique was first applied in the LMTO framework by Kudrnovsky and co-workers,[29,30] who used it to calculate the electronic structure of surfaces of random alloys within the LMTO coherent potential approximation framework,[31] and our implementation of the technique essentially follows theirs. It has also recently been used by MacLaren *et al.*[32] and Crampin *et al.*[33] The principal layer technique has the advantage that the computational effort scales linearly with the number of so-called principal layers as opposed to the close to cubic scaling of conventional approaches. Thus we are able to study interfaces with at least 100 atomic layers within reasonable computer times.

A. The principal layer technique for interfaces

The starting point of an interface Green's function calculation is the self-consistent one-electron potentials for the perfect crystals which are to be separated by the interface. Once these potentials have been obtained from a second-order LMTO eigenvalue problem, one proceeds to account for the changes in potential and structure near the interface by Dyson's equation. It is an important feature of the Green's function technique that one may obtain all information of the electronic structure needed in a self-consistent total energy calculation from the Korringa-Kohn-Rostoker (KKR) ASA Green's function g^{α} defined by

$$g^{\alpha}(z,\mathbf{k}) = [P^{\alpha}(z) - S^{\alpha}(\mathbf{k})]^{-1}, \tag{3}$$

where $P^{\alpha}(z)$ is the potential function in the α representation at energy z and $S^{\alpha}(\mathbf{k})$ is the corresponding structure constant matrix at a particular Bloch vector $\mathbf{k}$.

In the case of an interface one may slice the interface region into a number of so-called principal layers. A principal layer consists of so many atomic planes parallel to the interface that hopping, as mediated by the structure constants S, only occurs between nearest-neighbor principal layers. In the most-localized tight-binding representation, i.e., $\alpha = \beta$, of Andersen and Jepsen,[24] the number of atomic planes in a principal layer of a monoatomic solid is two or three depending on the close-packing of the interface layers. Thus the inversion problem, which is the time-consuming part of a Green's function calculation, may have as low a dimension as (18×18) for non-f metals.

The principal layer technique may be introduced via the ideal Green's function $\tilde{g}$, defined as the matrix inverse of the tight-binding KKR ASA scattering equations for a semi-infinite crystal, i.e.,

$$\tilde{g}(z,\mathbf{k}_{||}) = [P(z) - S(\mathbf{k}_{||})]^{-1}. \tag{4}$$

Here and in the following we suppress the LMTO representation index and assume that potential functions, structure constants, and Green's functions are all in the most localized β representation. The ideal Green's function defined in (4) represents a perfect crystal terminated by $P^{\beta} = \infty$ rather than by a hard-wall potential and this termination corresponds roughly to a vacuum potential lying 1 Ry above the occupied bands.[27] In the principal layer technique the ideal Green's functions for the semi-infinite left-hand crystals and the semi-infinite right-hand crystals form the two boundary conditions which connect the interface region to the surrounding bulk.

As suggested by Kudrnovský and Drchal,[29] the ideal Green's function for a semi-infinite crystal may be obtained from Dyson's equation

$$\begin{aligned}\tilde{g}_{0,0}(z,\mathbf{k}_{||}) = [&P_0(z) - S_{0,0}(\mathbf{k}_{||}) \\ &-S_{0,-1}\tilde{g}_{-1,-1}(z,\mathbf{k}_{||})S_{-1,0}]^{-1},\end{aligned} \tag{5}$$

which connects an initially isolated principal layer of index 0 to a semi-infinite stack of principal layers represented by the ideal Green's function $\tilde{g}$ projected onto its top layer of index -1. Once connected, we recover the semi-infinite stack of principal layers for which $\tilde{g}_{0,0}$ is the top-layer projection of the ideal Green's function. For the surface of a perfect crystal, it is always possible to choose the principal layer so that $\tilde{g}_{0,0} = \tilde{g}_{-1,-1}$, and this identity may be introduced into (5) to give a quadratic matrix equation for the ideal Green's function of a semi-infinite crystal, which may be solved by iteration.

In those cases, where the lattice periodicity perpendicular to the interface is considerably larger than the width of a principal layer, one may apply (5) several times to stack on top the semi-infinite crystal n *different* principal layers that together form a sequence which is commensurable with the lattice periodicity. The condition for self-consistency then becomes $\tilde{g}_{n-1,n-1} = \tilde{g}_{-1,-1}$ and this approach was taken in the calculation of the (001) antiphase boundary of the DO_{22} structure where the width of a principal layer is two atomic planes each containing two atoms whereas the repeat unit consists of four atomic planes and contains eight atoms. It should be noted that once the ideal Green's function for a semi-infinite crystal is obtained, one may, by repeated application of (5), construct the ideal Green's function for any stacking of layers, irrespective of the potential and the structure of these layers. This is one of the great advantages of the principal layer technique.

The major steps in an interface calculation may now be described. In the first step, one calculates the top layer projection $\tilde{g}^L_{0,0}$ of the ideal Green's function for the left-hand semi-infinite crystal and the top layer projection $\tilde{g}^R_{N+1,N+1}$ of the ideal Green's function for the right-hand semi-infinite crystal by the quadratic equation (5). One then proceeds to add, one at a time, the N principal layers of the actual interface to the two semi-infinite crystals, thereby defining a left- and a right-hand sequence of semi-infinite stacks with corresponding sequences of ideal Green's functions. If we denote by $\tilde{g}^L_{i,i}$ the top layer projection of the ideal Green's function when i principal layers have been attached to the left-hand semi-infinite crystal we have, from (5),

$$\tilde{g}^L_{i,i}(z,\mathbf{k}_{||}) = [P_i(z) - S_{i,i}(\mathbf{k}_{||}) - S_{i,i-1}(\mathbf{k}_{||})\tilde{g}^L_{i-1,i-1}(z,\mathbf{k}_{||})S_{i-1,i}(\mathbf{k}_{||})]^{-1}, \tag{6}$$

where, running from left to right through the principal layers of the interface, $i = 1, 2, ..., N$. Similarly, we have, for the sequence starting from the right-hand side,

$$\tilde{g}^R_{i,i}(z,\mathbf{k}_{||}) = [P_i(z) - S_{i,i}(\mathbf{k}_{||}) - S_{i,i+1}(\mathbf{k}_{||})\tilde{g}^R_{i+1,i+1}(z,\mathbf{k}_{||})S_{i+1,i}(\mathbf{k}_{||})]^{-1}. \tag{7}$$

The two sequences $\tilde{g}^L$ and $\tilde{g}^R$ of ideal Green's functions are subsequently used to calculate that part of the interface Green's function which is diagonal in the principal layer indices. For a given principal layer i this is done by starting from an initially isolated principal layer for which one reestablishes the hopping, as mediated by the structure constants, onto the semi-infinite stacks on both sides of the principal layer. This is completely analogous to the procedure for connecting a single principal layer on top a semi-infinite stack. The Dyson equation for the diagonal part of the interface Green's function g becomes

$$g_{i,i}(z,\mathbf{k}_{||}) = [P_i(z) - S_{i,i}(\mathbf{k}_{||}) - S_{i,i-1}(\mathbf{k}_{||})\tilde{g}^L_{i-1,i-1}(z,\mathbf{k}_{||})S_{i-1,i}(\mathbf{k}_{||}) - S_{i,i+1}(\mathbf{k}_{||})\tilde{g}^R_{i+1,i+1}(z,\mathbf{k}_{||})S_{i+1,i}(\mathbf{k}_{||})]^{-1}. \tag{8}$$

The diagonal parts of the interface Green's function contain the information needed to calculate total energies. However, the off-diagonal parts of the interface Green's function are essential for the use of the linearized Dyson equation, which we use to speed up convergence in a self-consistent calculation. Once the diagonal part of the interface Green's function has been calculated, the off-diagonal parts may be obtained by matrix multiplication. This is so because the off-diagonal part of the Dyson equation which connects the left-hand semi-infinite stack terminated after principal layer i to the right-hand semi-infinite stack terminated after principal layer $i+1$ reads

$$g_{i,i+n}(z,\mathbf{k}_{||}) = \tilde{g}_{i,i}(z,\mathbf{k}_{||})S_{i,i+1}g_{i+1,i+n}(z,\mathbf{k}_{||}). \tag{9}$$

For the first superdiagonal blocks, i.e., $n = 1$, this equation involves only those diagonal parts of the Green's function already obtained in (8). However, once the $n = 1$ blocks have been calculated, the next $n = 2$ blocks may be obtained by a second application of (9) and this recursive process may be continued until the off-diagonal elements become insignificant. In the present application we have stopped at $n = 3$. The subdiagonal parts $g_{i,i-n}$ may be obtained in a similar manner.

The principal layer technique described above may be viewed as a piecemeal solution of Dyson's equation for the interface. If this interface consists of N principal layers, the procedure requires $3N - 2$ matrix inversions, the dimension of which is given by the number of basis functions, here typically nine *spd* orbitals, times the number of atomic layers in a principal layer. Thus the principal layer technique involves matrix inversions of minimal dimensions and scales linearly with the number of atomic layers parallel to the interface plane.

B. Details of the calculations

To initiate the interface procedure, we perform self-consistent bulk calculations by means of the second-order LMTO Hamiltonian and calculate the one-electron contribution to the kinetic energy by integrating the bulk Green's function on a complex energy contour. The contour is chosen as a semicircle and the integration performed by a Gaussian technique on a mesh of 16 points distributed exponentially so as to increase the sampling density near the Fermi level. Furthermore, although it is more time consuming, we use in the bulk calculations a Brillouin zone based on the two-dimensional (2D) zone of the fault structure and in the direction perpendicular to the plane of the 2D zone we use 400 $\mathbf{k}_\perp$ points. This large number is necessary because the Green's function for a fault structure is calculated by the principal layer technique and hence is completely converged in terms of $\mathbf{k}_\perp$. The one-electron potential is relaxed for a number of atomic layers in the vicinity of the fault. For all APB's on cube planes we used 31 cube planes, each containing two inequivalent atoms, while for the faults on the close-packed planes we included eight atomic planes, each containing four inequivalent atoms in the self-consistency. In a few cases, the interface region was increased to 12 atomic planes, changing the fault energies by less than 10%. For the (001) APB's, the outermost atomic planes included in the interface region are completely bulk like and do not contribute to the fault energies.

In the case of an ordered compound, one should ideally choose the radii of the atomic spheres so as to minimize the errors introduced by the ASA. One kind of error is related to the shape approximation inherent in the use of atomic spheres. For fcc based compounds this error may be minimized by choosing spheres of equal radii in which case the neglected interstitial regions of space and the size of the overlap between neighboring spheres are reduced to a minimum. The second kind of error is caused by describing the one-electron potential only within overlapping atomic spheres. The choice of equal sphere radii in a compound causes a discontinuity between the one-electron potential at the surfaces of neighboring atomic spheres. This discontinuity may be large, especially if the Wigner-Seitz radii of the elemental metals deviate appreciably. In the present bulk and interface calculations we have minimized the discontinuity by choosing the relative radii as close as possible to the ratio of the radii of the elemental metals without increasing the overlap region too much. This is in the spirit of the guidelines given by Andersen,[34] which aim at the best possible (spherically symmetric) description of the potential inside overlapping spheres.

The $\mathbf{k}_{||}$ integration is performed by means of the special points devised by Cunningham.[35] For the faults at the close-packed planes of the $L1_2$ structure, we used 16 points in one-fourth of the centered rectangular 2D Brillouin zone. Increasing the number of k points to 64 changed the fault energies of Cu_3Au by less than $\sim 2\%$. For the faults at the close-packed planes of the DO_{22} structure, we used 16 points in one-fourth of the primitive rectangular 2D Brillouin zone. For the (001) APB's we used 36 k points in one-eighth of the square 2D Brillouin zone.

To maintain charge neutrality the small excess charge ($< 10^{-4}$ electrons) of the fault region is placed at two sheets just outside the fault structure and the corresponding contribution to the one-electron potential and the total energy is included. In this manner, we take approximate account of the charge connected with the Friedel oscillations and ensure fast convergence of the antiphase boundary energies in terms of the region size.

All calculations included s, p, and d orbitals and the lattice parameters used in the fault calculations were obtained by minimization of the total energy of the perfect crystal. Finally, for exchange and correlation we used the local density functional of Ceperley and Alder[36] as parametrized by Perdew and Zunger,[37] except for the DO_{22} compounds Ni_3V and Pd_3V. For these compounds, we used the Vosko-Wilk-Nusair[38] parametrization of the local density functional by Ceperley and Alder to allow for spin-polarized calculations.

IV. RESULTS

In what follows we shall present APB and stacking fault energies calculated self-consistently by means of the interface Green's function technique. However, we have also applied frozen bulk potentials in conjunction with the force theorem as implemented by Crampin *et al.*[39] This approximate approach give energies which are within $\sim 5\%$ of the self-consistent results, except for a few cases where the deviations are 10–20%.

A. $L1_2$

In Table I we present the calculated stacking fault and antiphase boundary energies for a series of intermetallic compounds observed in the $L1_2$ structure. As expected from the relation to ordering energies, the noble-metal compounds have low antiphase boundary energies while Ni_3Si has the highest fault energies of the compounds considered. In this context the fault energies of Ni_3Al appears anomalously low relative to those of Ni_3Si and Pt_3Al. In fact, the weakly ordered noble-metal compounds have APB and fault energies which are comparable to the values found for the strongly ordered Ni_3Al.

TABLE I. Calculated and experimental Wigner-Seitz radius S_{WS} together with calculated antiphase boundary energies (APB), superlattice intrinsic stacking fault energies (SISF), and complex stacking fault energies (CSF) for selected $L1_2$ compounds. Wigner-Seitz radii are in Bohr and energies in mJ/m^2.

	S_{WS}		APB		SISF	CSF
Compound	Present	Expt.[a]	(001)	(111)		
Au_3Cu	2.987	2.943	48	157	119	220
Cu_3Au	2.755	2.763	69	309	199	369
Ni_3Si	2.588	2.588	640	752	466	842
Ni_3Al	2.628	2.634	137	240	147	308
Pt_3Al	2.932	2.862	673	663	617	769
Co_3Ti	2.674	2.667	280	301	175	222

[a] Reference 46.

In general, the relation to the ordering energies is not found to be well obeyed. Thus the energy of the faults that preserve the nearest neighbors of atoms at the interface, i.e., the (001) APB and the SISF, are only marginally smaller than the CSF and the (111) APB energies, although the fault geometries of the latter introduce neighbor bonds between minority atoms.

It should be noted that the APB energies of the noble-metal compounds are highly anisotropic. Thus the (001) APB energy is a factor $\sim$ 3–4 smaller than the (111) APB energy. For Cu_3Au this is in agreement with the observation of a preferential orientation of thermally produced APB's.[40] Recently, Morris[16] has estimated the anisotropy of the APB energy by studying the shape of grown-in domain networks in rapidly solidified Ni_3Al. This leads to an anisotropy ratio of 1.4 at the stoichiometric composition, which should be compared to the ratio 1.75 in the present study. The anisotropy of the antiphase boundary energy plays an essential role in theory of the anomalous yield stress behavior observed in Ni_3Al, since the ratio of the (111) to the (001) antiphase boundary energy enters into the energy criterion, derived by Yoo,[7] for cross slip to occur.

The high values of the (001) APB energy in Pt_3Al and Co_3Ti relative to the (111) APB energy is particularly interesting since these intermetallics belong to a special class of $L1_2$ compounds that show a large flow stress increase with decreasing temperature.[6,41,42] According to Wee *et al.*,[41] the flow stress behavior is caused by either a high APB energy on both the (001) and (111) planes or a low SISF energy. This will lead to sessile SISF dissociated superdislocations causing the flow stress increase with decreasing temperature, as observed in experiment. Similarly, Liu *et al.*[42] investigated Co_3Ti and found SISF dissociation to be dominant at low tempera-

TABLE II. Comparison between calculated antiphase boundary (APB) energies and experimental results taken from the compilation by Veyssière (Ref. 14). Vitek *et al.* (Ref. 19) used an empirical N-body potential of the Finnis-Sinclair type (FS). Paxton (Ref. 3) used the full potential LMTO method (FP LMTO) while Fu *et al.* (Ref. 8) used the full potential LAPW method (FLAPW). Both Paxton and Fu *et al.* employed the supercell approach with relaxation included, but also give values for the unrelaxed case here listed in paranthesis. All energies are in mJ/m^2.

	(001) APB				(111) APB				
Compound	Present	Expt.[a]	FLAPW[b]	FS[c]	Present	Expt.[a]	FLAPW[b]	FP LMTO[d]	FS[c]
Cu_3Au	69			52	309	39		160 (180)	54
Ni_3Si	640	250	707		752	250	625 (685)		
Ni_3Al	137	140	140	53	240	180	175	170 (220)	
Pt_3Al	673				663			560 (500)	
Co_3Ti	280	210			301	270			

[a] Reference 14.
[b] Reference 8.
[c] Reference 19.
[d] Reference 3.

tures. Although Wee *et al.* considered the possibility of a very low SISF energy, it is clear from Table I that the present calculations support the assumption of SISF dissociated superdislocations for Pt_3Al and Co_3Ti because of the high (001) and (111) APB energies. In fact, since the present calculations do not include the effect of relaxation, the (001) APB energy may very well be higher than the (111) APB energy since one would expect relaxations to be important only for the latter type of APB. This is in contrast to the anomalous yield compound Ni_3Al in which cross slip is known to occur.

Fu and Yoo[43] calculated the elastic constants of Pt_3Al and Ni_3Al using the FLAPW method. Based on the energy criterion derived by Yoo[7] for cross slip to occur, they found that the ratio of the (111) to the (001) antiphase boundary energy had to be larger than 1.47 for Pt_3Al. As may be seen from Table I, we find a ratio $\lesssim 1$ for Pt_3Al, which indicates that cross-slip pinning will not occur for Pt_3Al. In contrast, the elastic constants calculated by Fu and Yoo indicate a minimal APB anisotropy ratio of ~ 1 for cross slip to occur in Ni_3Al and this is fulfilled by the present APB energies in Table II.

Ni_3Si belong to the group of anomalous yield alloys[44] and the calculated APB energies lead to an anisotropy ratio of 1.18. However, compared to Cu_3Au and Ni_3Al the anisotropy in APB energies is relatively moderate, especially since one would expect relaxation effects, not included in the present calculations, to lower our calculated anisotropy ratios. Fu *et al.*[8] calculated elastic constants for Ni_3Si and their values lead to a minimal APB anisotropy ratio of 1.15 for cross slip to occur. Hence it is not possible from the present calculations to determine whether the criterion for cross slip is fulfilled. In addition, one may expect that effects of off-stoichiometric concentration and ternary additions will significantly alter the mechanical properties of Ni_3Si.

In Table II, the APB energies calculated in the present work are compared with results from previous studies, both experimental and theoretical. As noted in the Introduction, calculated APB and stacking fault energies are sparse. As for experimental values, a range of measurements for Ni_3Al exist, most of which have been obtained from samples containing ternary additions. In addition to the values in Table II, Dimiduk *et al.*[18] calculated the (111) APB energy of Ni_3Al to be 141 mJ/m^2 compared to the present value of 240 mJ/m^2 and the experimental value of 180 mJ/m^2. For the (001) APB energy of Ni_3Al the present result and the experimental value are in excellent agreement, while the calculated value by Vitek *et al.*[19] is low.

The largest deviations between the experimental results and the present APB energies are found in Cu_3Au and Ni_3Si. For Ni_3Si, it should be noted that all experimental APB energies are smaller than ~ 250 mJ/m^2 and that the method applied to determine APB energies, i.e., TEM of partial dislocations, becomes increasingly uncertain as the APB energy increases. Furthermore, in the case of Ni_3Si the elastic constants used to derive the fault energies were assumed to be identical to the elastic constants of the ternary compound Ni_3(Si, Ti). This assumption is by no means obvious, since Ni_3Ti is observed in the DO_{24} structure, which is based on a complex stacking sequence of close-packed planes. As for the (111) APB of Cu_3Au, the present calculation seems to be an overestimate compared to experiment, but so is the full potential LMTO value of Paxton,[3] and only the value of Vitek *et al.*[19] is in reasonable agreement with the experimental result. However, Vitek *et al.*[19] found isotropic APB energies for Cu_3Au, which does not agree with the observation by Marcinkowski and Zwell[40] of thermally produced cuboid domain networks.

It may be inferred from Table II that part of the deviation between the present calculation and the full potential results of Paxton[3] and Fu *et al.*[8] is caused by the neglect of relaxation in the present work and one would tend to attribute the remaining deviation to the use of the atomic-sphere approximation. However, the full potential calculations rely on the supercell geometry and therefore include an unknown energy of interaction between antiphase boundaries whereas the present technique gives the energy of a single antiphase boundary embedded in an infinite medium.

In Table III we compare the present stacking fault energies with previous theoretical and experimental results.

TABLE III. Same as Table II, but for complex (CSF) and superlattice intrinsic stacking faults (SISF).

	CSF					SISF			
Compound	Present	Expt.[a]	FLAPW[b]	FP LMTO[c]	FS[d]	Present	FLAPW[b]	FP LMTO[c]	FS[d]
Cu_3Au	369	13		260(270)	40	199		120	16
Ni_3Si	842		710			466	460		
Ni_3Al	308	250	225	240(300)	189	147	40	60	11
Pt_3Al	769			600(700)		617		560	

[a] Reference 14.
[b] Reference 8.
[c] Reference 3.
[d] Reference 19.

In addition to the values given in the table, Veyssière *et al.*[45] obtained an experimental value ~ 5–15 mJ/m^2 for the SISF energy of Ni_3Al using weak beam TEM and Dimiduk *et al.*[18] obtained, by embedded atom calculations, a value of 121 mJ/m^2 for the CSF of Ni_3Al. In the comparison between the present results and the full potential calculations, both the FP LMTO results[3] and the FLAPW results,[8] we find that in general the energies are comparable, except for the SISF value of Ni_3Al. However, there are order of magnitude deviations between the present calculations and the work of Vitek *et al.*[19] as well as the experimental value for the CSF energy of Cu_3Au and the SISF energy of Ni_3Al. In contrast, the experimental value for the CSF energy of Ni_3Al is in good agreement with the present result.

The work of Paxton[3] also includes LMTO ASA calculations of (111) APB energies. He concludes that the LMTO ASA values are clear overestimates compared to experiment and that this is caused by the ASA. In view of the present calculations it appears that this conclusion should be modified. First of all, the LMTO ASA calculations by Paxton rely on a supercell geometry and therefore include an unknown energy of interaction between stacking faults while the present technique gives the energy of a single fault embedded in an infinite medium. Furthermore, because of the Green's function technique the 2D k-space integration is somewhat better converged than the 3D integration of conventional energy band methods. Finally, we have calculated the APB energies at the average Wigner-Seitz radius which minimizes the total energy and chosen the relative Wigner-Seitz radii so as to minimize the errors of the ASA while Paxton employs equal radii. As a result, the errors of the ASA have been reduced and the APB energies are now 25–50% smaller than the LMTO ASA values obtained by Paxton.[3]

B. DO_{22}

We have calculated antiphase boundary and stacking fault energies of three vanadium based compounds Ni_3V, Pd_3V, and Pt_3V, which form in the DO_{22} structure. It is known from previous local spin-density calculations that Ni_3V is ferromagnetic in the cubic $L1_2$ structure but paramagnetic in the DO_{22} structure.[49] Furthermore, based on a band theory approach Williams *et al.*[50] predicted that Pd_3V should be ferromagnetic in the $L1_2$ structure with a moment of $1.4\mu_B$ per formular unit (f.u.). We find, in agreement with these calculations, that all three compounds are ferromagnetic in the $L1_2$ structure and paramagnetic in the DO_{22} structure, except for Pt_3V, which develops a small magnetic moment in the DO_{22} structure. In addition, we find, in agreement with Xu *et al.*,[49] that the exchange energy gained in the formation of a magnetic moment in the $L1_2$ structure is considerably smaller than the energy gained by the transition to the DO_{22} structure and as a result the DO_{22} structure is found to be the ground state in all three compounds. We note that the magnetic moment of Pt_3V in the DO_{22} structure is calculated to be zero at the experimental lattice constant. Hence the small moment predicted at the minimum of the total energy may be an artifact of the overestimated lattice constant. However, this is not the case for the magnetic moments calculated in the cubic $L1_2$ structure.

The spin-polarized structural energy calculations for Ni_3V, Pd_3V, and Pt_3V are presented in Table IV and compared with the calculated energy of the (001) antiphase boundary in the DO_{22} structure. It is seen that, although of similar magnitude, one may not in general identify the (001) APB energy with the structural energy difference, as it was assumed by Pei *et al.*[17] in their calculations for Ni_3V, and Co_3Ti. The three LMTO ASA calculations of the structural energy difference in Ni_3V agree quite well and apart from possible differences in k-point convergence, the 20% difference between them may be caused by the choice of sphere radii. Pei *et al.* used equal sphere radii while we used radii that minimized the errors of the ASA. Furthermore, Xu *et al.* used the experimental c/a ratio for the DO_{22} structure, while the ideal c/a ratio was kept both in the present work and in the work of Pei *et al.*

The calculated antiphase boundary and stacking fault energies in Ni_3V, Pd_3V, and Pt_3V are presented in Table V together with recent experimental results for the fault energies in Ni_3V.[20] The experimental APB energies were obtained at temperatures in the range from 600° C to 800° C and the APB energies were found to be strongly dependent on temperature, while the intrinsic stacking fault energy was nearly temperature independent. It is seen that, with the exception of the (001) APB energy, the agreement between the calculated and experimental fault energies in Ni_3V is quite remarkable.

TABLE IV. Calculated and experimental Wigner-Seitz radius S_{WS} together with the calculated magnetic moment M, the calculated structural energy ΔE_{str} of the cubic $L1_2$ structure relative to the tetragonal DO_{22} structure, and the calculated antiphase boundary energies (APB) for three vanadium based DO_{22} compounds. All calculations are based on the LMTO ASA method. Numbers in parentheses refer to calculations assuming paramagnetic $L1_2$. Wigner-Seitz radii are in Bohr, magnetic moments in μ_B/f.u., and energies in mRy per formula unit (f.u.).

	S_{WS}		M		ΔE_{str}		APB(001)
Compound	Present	Expt.[a]	DO_{22}	$L1_2$	Present	LMTO	Present
Ni$_3$V	2.638	2.632	0	0.8	31(35)	26[b](30)[b] (28)[c]	22
Pd$_3$V	2.907	2.848	0	1.2	8.0(21)		15
Pt$_3$V	2.944	2.864	0.5	1.3	5.1(19)		7.7

[a] Reference 46.
[b] Reference 49.
[c] Reference 17.

The disagreement as to the energy of the (001) APB constitutes a problem, since one would expect the calculation to be particularly accurate for this case where the neglect of atomic relaxations will cause a minimal error. Furthermore, François *et al.*[20] predominantly observe splitting on close-packed planes which would occur when the (001) APB energy exceeds the (111) APB energy. One may therefore question the low experimental value for the (001) APB in Ni$_3$V.

The APB energies in Pd$_3$V are of the same order of magnitude while the ISF energy is one order of magnitude smaller. It is known that the short-range order in disordered Pd$_3$V exhibits the cubic concentration waves typical of $L1_2$ ordering whereas the low temperature state is DO_{22}.[47] On the other hand, the short-range order above the order-disorder temperature in Ni$_3$V is dominated by the ordering vector $\frac{1}{2}\langle 210\rangle$ of the DO_{22} structure.[48] This qualitative difference in the short-range order in disordered alloys of the two compounds agrees well with the calculated difference in (001) APB energy. That is, the structural energy difference between the DO_{22} and the $L1_2$ structure is a factor of 4 larger for Ni$_3$V than for Pd$_3$V. For Pt$_3$V, the (001) APB energy is even lower than for Pd$_3$V and this is consistent with the observation of long-period superstructures in Pt$_3$V just below the order-disorder temperature.[51] It may be inferred from Table IV that the decrease in structural energy difference between the $L1_2$ and the DO_{22} structures in going from Ni$_3$V to Pt$_3$V is due to the corresponding increase in spin polarization, i.e., assuming a paramagnetic state would result in only a weak decrease in the structural energy difference from Ni$_3$V to Pt$_3$V.

V. CONCLUSIONS

We have calculated the energies of antiphase boundaries and stacking faults in six $L1_2$ and three DO_{22} intermetallic compounds. For the Cu-Au compounds, the values obtained in the present calculations are typically 50–100 % larger than those of a previous full potential LMTO calculation by Paxton[3] and one order of magnitude higher than the experimentally derived values. For Pt$_3$Al and Ni$_3$Al the discrepancy between the present results and the full potential calculations of Paxton is much smaller and appears to be dominated by the neglect of atomic relaxation in the present work. A similar conclusion is reached when comparing the FLAPW calculations to the present results for Ni$_3$Al and Ni$_3$Si. The *ab initio* calculations are all in good agreement with the few experimental values for Ni$_3$Al. We find that the compounds Pt$_3$Al and Co$_3$Ti have high APB energies on the close-packed as well as the cubic planes while the SISF energy is smaller. This supports the explanation proposed by Wee *et al.*[41] of the flow stress behavior of these compounds.

We find that the ground state of Ni$_3$V, Pd$_3$V, and Pt$_3$V is a DO_{22} structure which is paramagnetic for Ni$_3$V and Pd$_3$V but ferromagnetic for Pt$_3$V. In contrast, the $L1_2$ structure of lowest energy is found to be ferromagnetic in all three compounds. The calculated structural energy difference between the DO_{22} and the $L1_2$ structure in Ni$_3$V is in good agreement with earlier local (spin-) density calculations. We also found the expected decrease in (001) APB energy in going from Ni$_3$V to Pd$_3$V. Fi-

TABLE V. Antiphase boundary energies APB(001), APB(111)$_1$, and APB(111)$_2$, intrinsic stacking fault energies (ISF), and complex stacking fault energies (CSF) for the DO_{22} compounds Ni$_3$V, Pd$_3$V, and Pt$_3$V. All energies are in mJ/m^2.

	APB(001)		APB(111)$_1$		APB(111)$_2$		ISF		CSF
Compound	Present	Expt.[a]	Present	Expt.[a]	Present	Expt.[a]	Present	Expt.[a]	Present
Ni$_3$V	372	145	167	177	54	40	22	25	325
Pd$_3$V	209		154		139		24		283
Pt$_3$V	106		176		158		27		441

[a] Reference 20.

nally, in Ni_3V we found excellent agreement between the calculated fault energies and the experimental results obtained by François *et al.*,[20] except for the energy of the (001) APB where the calculated value is 2.5 times the experimental result.

Finally, we point out that transition-metal compounds and compounds with strong directional bonding do not, in general, obey simple rules derived by considering only nearest-neighbor pair interactions. Therefore one cannot assume APB anisotropy in transition-metal compounds. In fact, for the transition-metal compounds investigated here it is the rule rather than the exception to see APB energies of the same magnitude on (001) and (111) planes.

ACKNOWLEDGMENTS

The work of N.M.R. was supported by grants from the Danish Natural Science Foundation and the Danish Technical Science Foundation. The Center for Atomic-scale Materials Physics is sponsored by the Danish National Research Foundation. Part of the work was supported by grants from the Novo Nordisk Foundation and the Danish research councils through the Danish Center for Surface Reactivity.

---

[*] Present address: Department of Physics, University of Cincinnati, Cincinnati, Ohio 45221.

[1] A.K. Sinha, Trans. AIME **245**, 911 (1969).

[2] S. Amelinckx, in *Dislocations in Solids*, edited by F.R.N. Nabarro (North-Holland, Amsterdam, 1979), Vol. 2, p. 67.

[3] A.T. Paxton, in *Electron Theory in Alloy Design*, edited by D.G. Pettifor and A.H. Cottrell (The Institute of Materials, London, 1992), p. 158.

[4] M. Yamaguchi, V. Vitek, and D.P. Pope, Philos. Mag. A **43**, 1027 (1981).

[5] Y.Q. Sun and P.M. Hazzledine, in *Ordered Intermetallics—Physical Metallurgy and Mechanical Behaviour*, edited by C.T. Liu and R.W. Cahn (Kluwer, Dordrecht, 1992), p. 177.

[6] V. Paider, D.P. Pope, and V. Vitek, Acta Metall. **32**, 435 (1984).

[7] M.H. Yoo, Scr. Metall. **20**, 915 (1986).

[8] C.L. Fu, Y.-Y. Ye, and M.H. Yoo, in *High-Temperature Ordered Intermetallic Alloys V*, edited by I. Baker, R. Darolia, and J. D. Whittenberger, MRS Symposia Proceedings No. 288 (Materials Research Society, Pittsburgh, 1993), p. 21.

[9] H.L. Skriver and N.M. Rosengaard, Phys. Rev. B **43**, 9538 (1991).

[10] H.L. Skriver and N.M. Rosengaard, Phys. Rev. B **46**, 7157 (1992).

[11] N.M. Rosengaard and H.L. Skriver, Phys. Rev. B **47**, 12 865 (1993).

[12] S. Mirbt, H.L. Skriver, M. Aldén, and B. Johansson, Solid State Commun. **88**, 331 (1993).

[13] N.M. Rosengaard and H.L. Skriver, Phys. Rev. B **49**, 14 666 (1994).

[14] P. Veyssière, in *Ordered Intermetallics—Physical Metallurgy and Mechanical Behaviour* (Ref. 5), p. 165.

[15] J. Douin, P. Veyssière, and P. Beauchamp, Philos. Mag. A **54**, 375 (1986).

[16] D.G. Morris, in *Ordered Intermetallics—Physical Metallurgy and Mechanical Behaviour* (Ref. 5), p. 123, and references therein.

[17] S. Pei, T.B. Massalski, W.M. Temmerman, P.A. Sterne, and G.M. Stocks, Phys. Rev. B **39**, 5767 (1989).

[18] D.M. Dimiduk, S. Rao, T.A. Parthasarathy, and C. Woodward in *Ordered Intermetallics—Physical Metallurgy and Mechanical Behaviour* (Ref. 5), p. 237.

[19] V. Vitek, G.J. Ackland, and J. Cserti, in *Alloy Phase Stability and Design*, edited by G. M. Stocks, D. P. Pope, and A. F. Giamei, MRS Symposia Proceedings No. 186 (Materials Research Society, Pittsburgh, 1991), p. 237.

[20] A. François, G. Hug, and P. Veyssière, Philos. Mag. A **66**, 269 (1992).

[21] O.K. Andersen, Phys. Rev. B **12**, 3060 (1975).

[22] H.L. Skriver, *The LMTO Method* (Springer-Verlag, Berlin, 1984).

[23] O. Gunnarsson, O. Jepsen, and O.K. Andersen, Phys. Rev. B **27**, 7144 (1983).

[24] O.K. Andersen and O. Jepsen, Phys. Rev. Lett. **53**, 2571 (1984).

[25] O.K. Andersen, O. Jepsen, and D. Glötzel, in *Highlights of Condensed-Matter Theory*, edited by F. Bassani, F. Fumi, and M. P. Tosi (North-Holland, New York, 1985).

[26] O.K. Andersen, Z. Pawlowska, and O. Jepsen, Phys. Rev. B **34**, 5253 (1986).

[27] W.R.L. Lambrecht and O. K. Andersen, Surf. Sci. **178**, 256 (1986), and (private communication).

[28] F. Garcia-Moliner and V.R. Velasco, Prog. Surf. Sci. **21**, 93 (1986).

[29] J. Kudrnovský and V. Drchal, in *Studies in Surface Science and Catalysis*, edited by J. Koukal (Elsevier, Amsterdam, 1988), Vol. 36, p. 74.

[30] B. Wenzien, J. Kudrnovský, V. Drchal, and M. Šob, J. Phys. Condens. Matter **1**, 9893 (1989).

[31] J. Kudrnovsky, P. Weinberger, and V. Drchal, Phys. Rev. B **44**, 6410 (1991).

[32] J.M. MacLaren, X.-G. Zhang, A. Gonis, and S. Crampin, Phys. Rev. B **40**, 9955 (1989).

[33] S. Crampin, J.B.A.N. van Hoof, M. Nekovee, and J. Inglesfield, J. Phys. Condens. Matter **4**, 1475 (1992).

[34] O.K. Andersen (unpublished).

[35] S.L. Cunningham, Phys. Rev. B **10**, 4988 (1974).

[36] D.M. Ceperley and B.J. Alder, Phys. Rev. Lett. **45**, 566 (1980).

[37] J. Perdew and A. Zunger, Phys. Rev. B **23**, 5048 (1981).

[38] S.H. Vosko, L. Wilk, and M. Nusair, Can J. Phys. **58**, 1200 (1980).

[39] S. Crampin, K. Hampel, D.D. Vvedensky, and J.M. MacLaren, J. Mater. Res. **5** (10), 2107 (1990).

[40] M.J. Marcinkowski and L. Zwell, Acta Metall. **11**, 373 (1963).

[41] D.M. Wee, D.P. Pope, and V. Vitek, Acta Metall. **32**, 829 (1984).

[42] Y. Liu, T. Takasugi, O. Izumi, and T. Takahashi, Philos. Mag. A **59**, 423 (1989).

[43] C.L. Fu and M.H. Yoo, Philos. Mag. Lett. **58**, 199 (1988).

[44] T. Takasugi and M. Yoshida, Philos. Mag. A **65**, 613 (1992).

[45] P. Veyssière, J. Douin, and P. Beauchamp, Philos. Mag. A **51**, 469 (1985).

[46] W.B. Pearson, *Handbook of Lattice Spacings and Structures of Metals* (Pergamon, New York, 1958), Vol. 1; *ibid.* (Pergamon, New York, 1967), Vol. 2.

[47] F. Solal, R. Caudron, F. Ducastelle, A Finel, and A. Loiseau, Phys. Rev. Lett. **58**, 2245 (1987).

[48] F. Solal, R. Caudron, and A. Finel, Physica B **156&157**, 75 (1989).

[49] J.-H. Xu, T. Oguchi, and A.J. Freeman, Phys. Rev. B **35**, 6940 (1987).

[50] A.R. Williams, R. Zeller, V.L. Moruzzi, and C.D. Gelatt, Jr., J. Appl. Phys. **52**, 2067 (1981).

[51] D. Schryvers and S. Amelinckx, Acta Metall. **34**, 43 (1986).

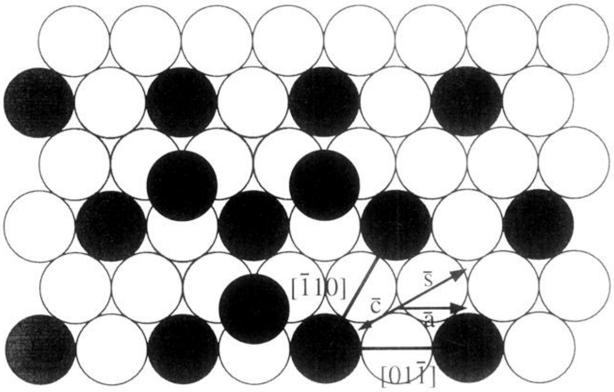

FIG. 1. Close-packed plane in the $L1_2$ structure. Shaded circles indicate the position of minority atoms, while open circles denote the position of majority atoms. Light shaded circles and dark circles indicate position of minority atoms in the close-packed layers below and above. Fault vectors of the (111) APB, the complex (CSF), and superlattice intrinsic (SISF) stacking faults are shown as $\bar{a}$, $\bar{c}$, and $\bar{s}$, respectively.

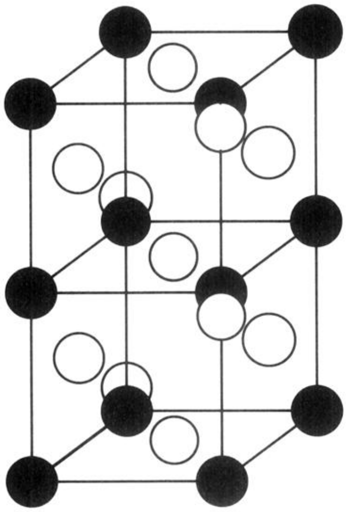

FIG. 2. Two unit cells of the $L1_2$ crystal structure stacked along the [001] cube axis. Filled spheres indicate the position of minority atoms and open spheres indicate the position of majority atoms. Viewed along the cube axis every second layer consists of majority atoms only.

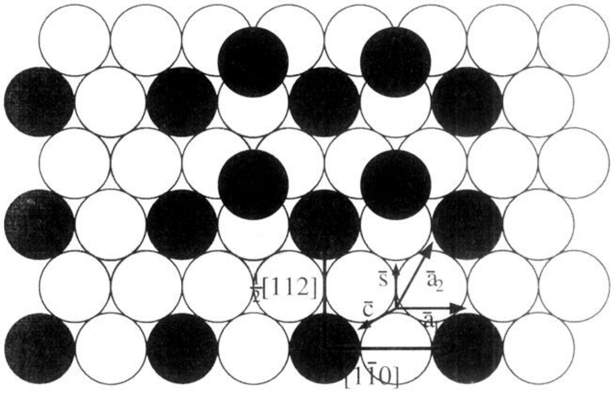

FIG. 3. Close-packed plane in the DO_{22} structure. Shaded circles indicate the position of minority atoms, while open circles denote the position of majority atoms. Light shaded circles and dark circles indicate position of minority atoms in the close-packed layers below and above. Fault vectors of the (111) APB's, the complex (CSF), and the simple intrinsic (ISF) stacking faults are shown as $\bar{a}_1$, $\bar{a}_2$, $\bar{c}$, and $\bar{s}$, respectively. The two lattice vectors shown represent Burgers vectors for observed superdislocations.